ACS OMEGA

http://pubs.acs.org/journal/acsodf

Article

Synergistic Effect of MIL-101/Reduced Graphene Oxide Nanocomposites on High-Pressure Ammonia Uptake

Cheongwon Bae,[§] Gyuyeong Jeong,[§] Suhyeon Park, Yeram Kim, Mingyu Gu, Duckjong Kim,* and Juyeong Kim*

Cite This: *ACS Omega* 2022, 7, 17144−17150

Read Online

ACCESS | Metrics & More | Article Recommendations | Supporting Information

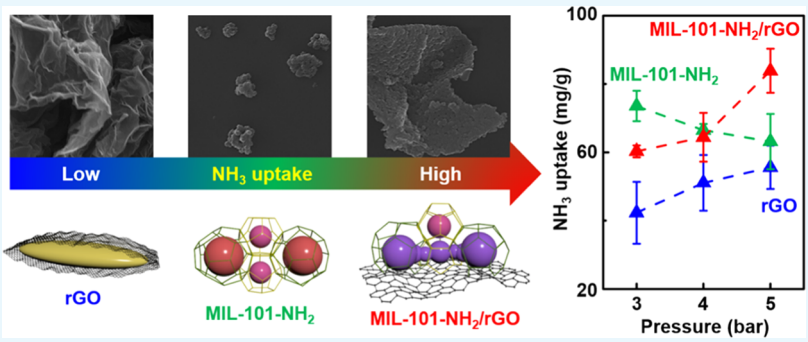

ABSTRACT: Ammonia has emerged as a potential working fluid in adsorption heat pumps (AHPs) for clean energy conversion. It would be necessary to develop an efficient adsorbent with high-density ammonia uptake under high gas pressures in the low-temperature range for waste heat. Herein, a porous nanocomposite with MIL-101(Cr)-NH_2 (MIL-A) and reduced graphene oxide (rGO) was developed to enhance the ammonia adsorption capacity over high ammonia pressures (3−5 bar) and low working temperatures (20−40 °C). A one-pot hydrothermal reaction could form a two-dimensional sheet-like nanocomposite where MIL-A nanoparticles were well deposited on the surface of rGO. The MIL-A nanoparticles were shown to grow on the rGO surface through chemical bonding between chromium metal centers in MIL-A and oxygen species in rGO. We demonstrated that the nanocomposite with 2% GO showed higher ammonia uptake capacity at 5 bar compared with pure MIL-A and rGO. Our strategy to incorporate rGO with MIL-A nanoparticles would further be generalizable to other metal−organic frameworks for improving the ammonia adsorption capacity in AHPs.

1. INTRODUCTION

Ammonia has emerged as an alternative tool to realize carbon-free energy conversion.[1−4] Ammonia is composed of three hydrogen atoms and one nitrogen atom, and it can be utilized as a potential hydrogen carrier for fuel cells.[5−7] Ammonia can be stored and transported more efficiently and safely than hydrogen because of its easy liquefication and high specific mass density of hydrogen atoms.[8] In addition, ammonia has become a great candidate as a working fluid in adsorption heat pumps (AHPs).[1,4,9] In contrast to conventional heat pumps that adapt an electrical condenser with hydrofluorocarbon as a refrigerant, environmentally friendly heat sources such as waste heat and solar heat are applied to the AHPs with water, alcohol, or ammonia as working fluid.[10] Ammonia is considered as the most advantageous working fluid for achieving high performance in the AHPs, in terms of its high vapor pressure and mass transfer.[11] Developing an adsorbent with high ammonia uptake capacity under high pressures and low temperatures will help to realize carbon-free energy conversion systems.

Inorganic materials such as metal halides, zeolites, and silica have been commonly used as adsorbents for ammonia.[11−14] Metal halides could easily form metal−ammine complexes with ammonia through chemical equilibrium.[3] In spite of their high adsorption capacity for ammonia, metal halides showed low durability to repeated ammonia adsorption and desorption cycles because of salt swelling and agglomeration.[15] Zeolite and silica have shown improvement in structural durability,[16,17] while the adsorbed amount of ammonia could not exceed that of metal halide salts.[11,12] Therefore, it is necessary to develop an efficient adsorbent that accommodates both advantages, structural stability and high adsorption capacity for ammonia.

Received: February 5, 2022
Accepted: May 4, 2022
Published: May 12, 2022

There has been much effort to seek metal−organic frameworks (MOFs) that can have high ammonia uptake capacity and durability at various ammonia pressures.[18−20] MOFs are composed of metal nodes and organic linkers, and they have shown great specific surface area in contrast to conventional inorganic porous materials.[21] A variety of these building units provide diversity in the pore size, geometry, and chemical property. Precise control of complex interactions between MOFs and ammonia molecules in terms of specific surface area, functional groups in the linker, and open metal sites in the secondary building unit would be considered for improving the ammonia adsorption performance.[22−26] However, the ammonia adsorption capacity by MOFs has not been superior to that reported by metal halide salts, and there have been a few reports that investigated ammonia uptake performance with MOFs at high ammonia pressures at low working temperatures corresponding to waste heat.

Herein, we introduced graphene oxide (GO) to MIL-101(Cr)-NH_2 (MIL-A) and developed a nanocomposite that consisted of MIL-A nanoparticles and reduced graphene oxide (rGO) sheets. MIL-A/rGO nanocomposites with different contents of GO were investigated for ammonia uptake capacity under high ammonia pressures (3−5 bar) and low working temperatures (20−40 °C). MIL-A was selected because of its high specific surface area and ammine group on its linker that could function as an adsorption site for ammonia through hydrogen bonding.[27−29] The introduction of GO or rGO on MOFs has shown synergistic effects on gas adsorption, separation, and sensing due to unique interfacial nanostructures and enhanced conductivity.[30−35] A composite between a copper-based MOF and GO could have more unsaturated copper sites and small micropores at the heterogeneous interfaces, which allowed excellent CO_2 uptake.[32] In addition, polypyrrole-coated rGO could improve the electrical conductivity of Cu-BTC MOF for ammonia sensing, where BTC stands for benzene-1,3,5-tricarboxylate.[34] Thus, such structural properties would be anticipated in the MIL-A/rGO nanocomposite for high-pressure ammonia adsorption. It was found that incorporation of rGO sheets to MIL-A nanoparticles could generate mesoscale interfacial cavities between MIL-A and rGO, which eventually allowed the nanocomposite to have the highest ammonia uptake at 5 bar than homogeneous MIL-A and rGO, respectively.

2. EXPERIMENTAL SECTION

2.1. Chemicals. Chromium nitrate nonahydrate (99%, $Cr(NO_3)_3{\cdot}9H_2O$, Sigma-Aldrich), 2-aminoterephthalic acid (99%, $C_8H_7NO_4$, Alfa Aesar), sodium hydroxide (99.99%, NaOH, Sigma-Aldrich), 1% graphene oxide aqueous solution (10 g/L, Grapheneall Co., Ltd.), methyl alcohol (99.5%, CH_3OH, Daejung), *N*,*N*-dimethylformamide (>99.8%, $HCON(CH_3)_2$, Daejung), and ammonia gas (99.9995%, NH_3, Daesung Industrial Gases Co., Ltd.) were purchased and used without further purification. Deionized water (18.2 MΩ·cm at 25 °C) purified by a Merck Millipore Direct Q3 UV Water Purification System was used for all washing and aqueous solution preparation. Autoclave Teflon containers were treated with aqua regia (a mixture of HCl and HNO_3 with a volume ratio of 3:1) and 3 M NaOH repeatedly, washed with deionized water, and dried immediately before use.

2.2. Synthesis of MIL-A/rGO Nanocomposites. MIL-A/rGO nanocomposites with different GO ratios were prepared according to the literature method with modifications.[36] An aqueous solution of GO was diluted with deionized water in a 200 mL Teflon container, where the volume of the GO solution was set as follows: 0 mL for MIL-A/rGO (0%), 1 mL for MIL-A/rGO (1%), 2 mL for MIL-A/rGO (2%), 4 mL for MIL-A/rGO (4%), 8 mL for MIL-A/rGO (8%), and 100 mL for MIL-A/rGO (100%). The total volume of the diluted GO solution was adjusted to 80 mL under each condition by adding deionized water, excluding MIL-A/rGO (100%). $Cr(NO_3)_3{\cdot}9H_2O$ (5.334 g for 0%, 5.281 g for 1%, 5.175 g for 2%, 4.968 g for 4%, and 4.571 g for 8%) and 2-aminoterephthalic acid (2.400 g for 0%, 2.376 g for 1%, 2.328 g for 2%, 2.235 g for 4%, and 2.057 g for 8%) were added to the diluted GO solution and dissolved well, respectively. Each solution was mixed well by a homogenizer at 8000 rpm for 10 min. NaOH (1.332 g for 0%, 1.319 g for 1%, 1.306 g for 2%, 1.279 g for 4%, and 1.226 g for 8%) in 20 mL of deionized water was added into the mixture during the homogenizing. After 2 min, the mixture in a Teflon container was sealed in a stainless steel autoclave. It was placed in an oven at 150 °C for 12 h for the hydrothermal reaction. Then, it was cooled down at room temperature for 6 h and transferred into six 50 mL conical tubes by ∼16 mL. It was centrifuged at 5000 rcf for 10 min, and the supernatant was removed as much as possible. The remaining product was dispersed with 40 mL of *N*,*N*-dimethylformamide and centrifuged at 5000 rcf for 10 min. After the supernatant was removed, the remaining product was dispersed with 100 mL of methyl alcohol and transferred into a 200 mL Teflon container. It was sealed in a stainless steel autoclave and placed in an oven at 100 °C for 24 h. Then, it was cooled down at room temperature for 6 h. It was transferred into six 50 mL conical tubes by ∼16 mL. It was centrifuged at 5000 rcf for 10 min, and the supernatant was removed as much as possible. The remaining product was dispersed with 40 mL of methyl alcohol and centrifuged at 5000 rcf for 10 min. The wet product was transferred into a 50 mL vial and dried in an oven at 80 °C for 12 h. Note that the nanocomposite with the GO ratio higher than 8% was formed as aerogels instead of particulates. MIL-A/rGO (100%) was broken into pieces as much as possible before characterization to avoid any influence from the macroscopic difference.

2.3. Characterization. All samples were characterized after being treated at 80 °C under vacuum for 6 h. An FEI Tecnai TF30ST transmission electron microscope (TEM) with a ZrO/W(100) Schottky emitter at 300 kV was used for material characterization. A JEM-ARM200F Cs-corrected scanning transmission electron microscope (JEOL) was used for elemental mapping. A small amount of sample was dispersed in 1 mL of ethyl alcohol by sonication for 5 min, and the sample solution (10 μL) was dropped and dried on a TEM grid before TEM imaging. A TESCAN S8000 scanning electron microscope (SEM) was used for analyzing morphology. The sample solution (20 μL) was dropped and dried on a silicon wafer (0.5 cm × 0.5 cm) before SEM imaging. A D8 Advanced A25 (BRUKER) was used for powder X-ray diffraction (XRD) measurement. Infrared (IR) spectra were obtained using a Nicolet iS5 FTIR spectrometer (Thermo Fisher Scientific) with iD7 ATR Accessory. Raman spectra were measured by a DXR2xi Raman imaging microscope (Thermo Fisher Scientific) with a DXR 532 nm filter. A Belsorp-mini II (MicrotracBEL) was used to analyze the Brunauer−Emmett−Teller (BET) surface area and the Barrett−Joyner−Halenda (BJH) pore distribution. N_2 adsorption and desorption were measured at 77.5 K.

https://doi.org/10.1021/acsomega.2c00741
ACS Omega 2022, 7, 17144−17150

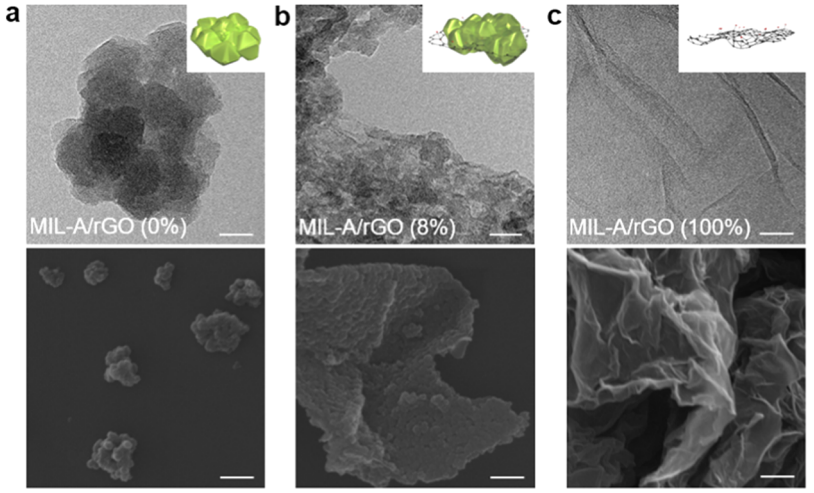

Figure 1. Electron microscopy images of MIL-A/rGO nanocomposites with different GO ratios (0% for (a), 8% for (b), and 100% for (c)). TEM images are in the upper row, and SEM images are in the bottom row. Scale bar: 30 nm in TEM images and 300 nm in SEM images.

2.4. Ammonia Adsorption Measurement. All samples were characterized after being treated at 80 °C under vacuum for 6 h. The dried sample (0.2 g) was placed and sealed tightly in a 125 mL chamber of our customized high-pressure gas sorption analyzer. The chamber temperature was adjusted to 39.95 ± 0.32 °C by heating tape connected to a proportional−integral−differential (Hanyoung Nux, VX7-USNA-A2) (PID) controller with a thermocouple (Omega Engineering, ±0.2% FS) while ammonia gas flowed into the chamber. The initial charge pressure was adjusted to between 3 and 5 bar, and it was sufficiently held until stabilized at the targeted pressure. After stabilization of the gas pressure, the heating tape was turned off and the chamber was cooled with water at 20.02 ± 0.18 °C driven by a bath circulator (Jeio Tech, RW3-3025P, ±0.05 °C). When the gas pressure in the cooled chamber was stabilized, the ammonia pressure drop in the chamber was measured by a pressure sensor (Sensys, PSCD0015BCPG-W, 0−15 bar, ±0.25% FS) and acquired by a data acquisition system (Keysight, DAQ970A). Manometric measurements between 40 and 20 °C were converted as the mass of adsorbed ammonia by the ideal gas law. Note that any ammonia pressure drop by the chamber wall from 40 to 20 °C was excluded in calculating the amount of adsorbed ammonia.

3. RESULTS AND DISCUSSION

MIL-A/rGO nanocomposites were synthesized with different GO ratios, and their nanoscale structures were characterized by electron microscopic measurements (Figures 1, S1, and S2). As the GO ratio increased, MIL-A/rGO nanocomposites transformed from particulate-like to sheet-like agglomerates. Pure MIL-A without GO was formed as particulate-like agglomerates with 131.0 ± 96.4 nm in diameter, which were composed of individual polyhedral nanoparticles with 30.7 ± 11.8 nm in length (Figures 1a and S3). On the other hand, MIL-A/rGO (8%) was formed as two-dimensional (2D) sheet-like agglomerates (Figure 1b), which resembled the shape of 2D rGO sheets without MIL-A (Figure 1c). Unlike pure rGO sheets without MIL-A, MIL/rGO (8%) contained rough surfaces that corresponded to the MIL-A nanoparticles. MIL-A nanoparticles in MIL-A/rGO (8%) seemed to be mingled well with the rGO sheets. Elemental mapping also demonstrated the uniform distribution of chromium from MIL-A nanoparticles over the rGO sheets in MIL/rGO (8%) (Figure S4). MIL-A nanoparticles could be readily nucleated and grown on the rGO sheets during the hydrothermal reaction, resulting in the facile deposition of MIL-A nanoparticles on the rGO surface. The size of MIL-A nanoparticles in MIL-A/rGO (8%) was measured as 27.6 ± 8.8 nm (Figure S3), slightly smaller than that of pure MIL-A. The presence of GO may have an influence on the nucleation and growth of MIL-A nanoparticles.

The crystallinity of MIL-A/rGO nanocomposites with different GO ratios was confirmed by XRD (Figure 2). All

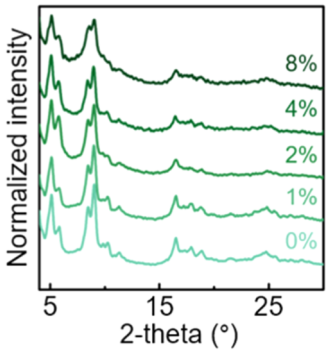

Figure 2. XRD patterns of MIL-A/rGO nanocomposites with different GO ratios (from bottom to top: 0, 1, 2, 4, and 8%).

nanocomposites showed the representative XRD peaks for the porous periodic framework of MIL-A, at 5.1° for {511}, 5.8° for {531}, 8.5° for {660}, and 9.0° for {753}.[37] The full width at half-maximum (FWHM) between 8.5 and 9.0° appeared to increase as the GO ratio in the nanocomposite increased, implying the size decrease of MIL-A nanoparticle.[38] It could be ascribed that the GO sheets provided more nucleation sites for MIL-A than in the absence of GO and consequently promoted the formation of smaller MIL-A nanoparticles. According to the literature,[39,40] GO could induce distortion in the MOF growth when the nanocomposite between MOF and GO was formed. We assumed that such interruption could lead to changes in MIL-A nanoparticle size along with the MIL-A crystallinity.

https://doi.org/10.1021/acsomega.2c00741
ACS Omega 2022, 7, 17144−17150

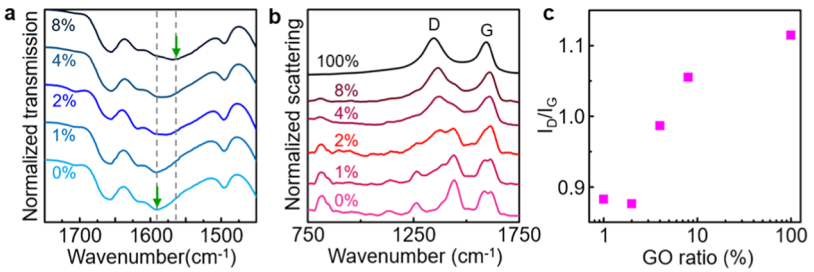

Figure 3. (a) IR spectra of MIL-A/rGO nanocomposites with different GO ratios (from bottom to top: 0, 1, 2, 4, and 8%). (b) Raman spectra of MIL-A/rGO nanocomposites with different GO ratios (from bottom to top: 0, 1, 2, 4, 8, and 100%). (c) Correlation plot with the peak intensity ratios between the D band and G band as a function of the GO ratio. The dotted lines are a guide to the eye.

Bonding interactions between MIL-A and rGO in the nanocomposite were investigated by IR spectroscopy (Figures 3a and S5). The characteristic vibration modes of the amine group in the linker of MIL-A were shown at 1340 cm^{-1} for CN stretching, 1618 cm^{-1} for NH bending, 3350 cm^{-1} for symmetric NH stretching, and 3462 cm^{-1} for asymmetric NH stretching (Figure S5),[36,41] and there was no significant shift in these peaks of the nanocomposites with different GO ratios. Since the amine group could be sensitive to intermolecular interaction such as hydrogen bonding or acid−base reaction,[42] we could presume that the chemical environment inside the micropore of MIL-A was not affected by the compositing with GO. However, the asymmetric stretching mode of the carboxylic acid group in the linker was shown to red-shift from 1592 cm^{-1} for pure MIL-A to 1569 cm^{-1} for the nanocomposite with 8% of GO (Figure 3a). The interfacial interaction between MIL-A and rGO was likely to emerge in the nanocomposite with higher GO ratios, led by additional bonds formed between carboxylates on the surface of rGO and undercoordinated chromium metal center from MIL-A. Our control experiment from the hydrothermal reaction between chromium precursor and GO revealed an apparent redshift of the asymmetric stretching mode of a carboxylic acid group to 1560 cm^{-1} (Figure S6). This supported that the redshift of the asymmetric stretching mode in the MIL-A/rGO nanocomposite could be attributed to coordination between carboxylates of GO and chromium of MIL-A formed during the hydrothermal reaction, implying that GO served as nucleation sites for MIL-A nanoparticles.

In addition, we examined the characteristic signals of rGO in the nanocomposites with different GO ratios via Raman spectroscopy (Figure 3b). Pure rGO clearly displayed the D band at 1347 cm^{-1} and the G band at 1593 cm^{-1}, originating from the aromatic ring in the rGO sheets.[43] The relative intensity ratio of the D and G bands, I_D/I_G, could be investigated to evaluate the structural deficiency of rGO (Figure 3c).[44] The D band intensity is known as proportional to the degree of defects in graphene, and the G band refers to sp^2 carbon atoms in the six-membered aromatic ring.[45,46] The I_D/I_G value increased from 0.88 with MIL-A/rGO (1%) to 1.11 with pure rGO, demonstrating that the rGO structure in the nanocomposite has fewer defective sites than pure rGO. In other words, the presence of MIL-A nanoparticles could reduce the formation of defects on the GO sheet during the hydrothermal reaction, in that predominant incorporation between GO and MIL-A could prohibit chemical reduction of GO with more defects on the six-membered ring structure in the hydrothermal process.

The porous properties of the nanocomposites with different GO ratios were examined from N_2 physisorption (Figure 4).

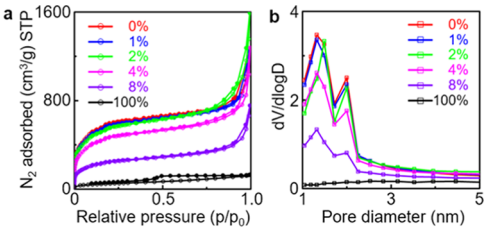

Figure 4. (a) Isotherm linear plots for N_2 physisorption with MIL-A/rGO nanocomposites (GO ratio: 0, 1, 2, 4, 8, and 100%). (b) Pore diameter distribution with MIL-A/rGO nanocomposites (GO ratio: 0, 1, 2, 4, 8, and 100%).

The N_2 isotherms of the nanocomposites showed that their porosity belonged to type I with micropores mostly originating from MIL-A,[47] whereas the porosity of pure rGO was classified as type IV with dominant mesopores (Figure 4a).[48] As the GO ratio in the nanocomposite increased, its BET surface area gradually decreased, e.g., by ∼58% from 1934 m^2/g for pure MIL-A to 812 m^2/g for MIL-A/rGO (8%) (Table S1). The addition of GO gave rise to a decrease in the number of micropores in MIL-A, while the mass fraction of GO in the nanocomposite could not be more dominant than that of MIL-A. Such large reduction in the BET surface area of MIL-A/rGO (8%) could be attributed to the increase in the mesoporosity of rGO as well as distortion in the micropores of MIL-A by the addition of GO. Although the BET surface area decreased upon compositing MIL-A with GO, the adsorption capacity, excluding that by the micropores in the low relative pressures up to 0.3 in P/P_0, was shown as the highest for MIL-A/rGO (2%), 501 cm^3/g, followed by pure MIL-A, 321 cm^3/g, and MIL-A/rGO (4%), 319 cm^3/g. Such high adsorption capacity in MIL-A/rGO (2%) was also represented with its larger pore diameter and total pore volume than the other nanocomposites (Figure 4b and Table S1). According to the literature,[49−51] the adsorption at the relative pressure from 0.300 to 0.962 could occur through capillary condensation of adsorbates, where mesoscale cavities would play a critical role. We anticipated that such mesoscale cavities would be beneficial for increasing adsorption capacity, facilitating the storage of gas molecules.

Ammonia adsorption capacity by the nanocomposites with different GO ratios in the temperature range (20−40 °C), corresponding to waste heat utilization was measured by our customized high-pressure gas sorption analyzer (Figure 5 and Table S2). We could measure the amount of ammonia

https://doi.org/10.1021/acsomega.2c00741
ACS Omega 2022, 7, 17144−17150

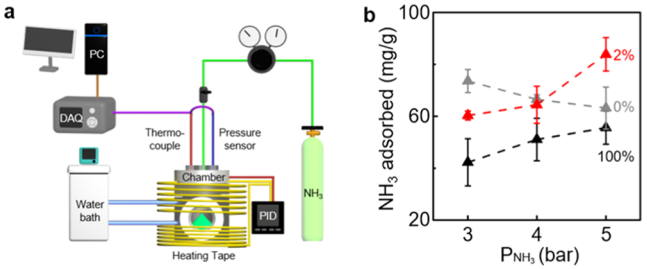

Figure 5. (a) Schematic representation of our customized high-pressure ammonia sorption analyzer. (b) Ammonia uptake at different ammonia pressures with MIL-A/rGO nanocomposites (GO ratio: 0, 2, and 100%).

molecules that reversibly adsorb and desorb at temperature swings under a high ammonia pressure (Figure 5a). The initial ammonia gas pressure in the chamber was first adjusted to between 3 and 5 bar at 40 °C, and pressure drop during cooling to 20 °C was measured and transformed to the amount of adsorbed ammonia molecules. Note that there was little influence of GO in MIL-A/rGO (2%) for the ammonia adsorption since most GO could be reduced to rGO during the hydrothermal reaction (Figure S6). As the initial ammonia pressure increased from 3 to 5 bar (Figure 5b), the ammonia uptake increased for MIL-A/rGO (2%) and pure rGO. However, pure MIL-A showed a gradual decrease in the adsorption capacity according to the increase in the ammonia pressure. It was presumed that such discrepancy in the ammonia adsorption capacity could be attributed to the pressure-relevant interplay between the ammonia and micropores of MIL-A and mesoscale cavities at the interface between MIL-A and rGO. Thus, we supposed that the ammonia adsorption capacity in the pressure range between 3 and 4 bar at 20 °C could be highly dependent on the specific surface area, as pure MIL-A retained more micropores than MIL-A/rGO (2%) and pure rGO. On the other hand, MIL-A/rGO (2%) with more mesoscale cavities displayed the highest ammonia uptake capacity in the pressure range between 4 and 5 bar, where dispersive forces would play a significant role in the increase of the ammonia adsorption capacity.[31,34] In addition, we assumed that preadsorbed ammonia molecules at 40 °C under 4−5 bar could be more in pure MIL-A than MIL-A/rGO (2%) (Figure S7), contributing to the higher ammonia uptake of MIL-A/rGO (2%). The nanocomposite of MIL-A/rGO (2%) could contain the mesoscale cavities formed between the MIL-A nanoparticle and the rGO sheet along with the micropores from MIL-A, which gave rise to a synergistic effect on the ammonia adsorption at higher pressures in the temperature range for waste heat utilization. The IR spectra before and after the ammonia adsorption on MIL-A/rGO (2%) were almost identical, demonstrating its structural stability (Figure S8).

4. CONCLUSIONS

The nanocomposite of MIL-A and rGO could be developed with different GO ratios through a one-pot hydrothermal reaction. As the GO content increased, the morphology of MIL-A/rGO transformed from particulate-like aggregates to 2D sheet-like aggregates. During the formation process of MIL-A, the GO sheets could function as nucleation sites for MIL-A nanoparticles, resulting in their deposition on the rGO surface and slight size reduction. There was a gradual redshift of the asymmetric stretching mode of the carboxylic acid group of the linker in MIL-A when the GO ratio increased, which could indicate chemical bondings between uncoordinated chromium metal centers of MIL-A and oxygen species on the surface of rGO. The presence of MIL-A also played a role in suppressing the formation of defects on the six-membered carbon rings in the GO against further reduction by hydrothermal reaction. As the GO ratio in the nanocomposite increased, its BET surface area decreased due to the nonmicroporosity of the rGO. However, the total pore volume and the capillary condensation-based adsorption became the highest with MIL-A/rGO (2%) compared to pure MIL-A. Furthermore, MIL-A/rGO (2%) showed the highest ammonia uptake capacity at 5 bar in the low-working-temperature range. Such outstanding performance could be attributed to the unique hybrid porous structure in the nanocomposite, mesocavities generated at the interfaces between MIL-A and rGO along with the micropores from MIL-A, which appeared to allow higher dispersive force for ammonia molecules under high pressures. Our demonstration would help find a way to improve high-pressure ammonia uptake capacity with MOFs by incorporating graphene oxides.

■ ASSOCIATED CONTENT

Supporting Information

The Supporting Information is available free of charge at https://pubs.acs.org/doi/10.1021/acsomega.2c00741.

TEM images of MIL-A/rGO, SEM images of MIL-A/rGO, length distribution of MIL-A/rGO, STEM EDS images of MIL-A/rGO, full IR spectra of MIL-A/rGO, IR spectra of GO treated under different conditions, schematics of ammonia adsorption mechanisms, and full IR spectra of MIL-A/rGO after ammonia uptake (PDF)

■ AUTHOR INFORMATION

Corresponding Authors

Duckjong Kim − *Department of Mechanical Engineering, Gyeongsang National University, Jinju 52828, South Korea*; Email: dkim@gnu.ac.kr

Juyeong Kim − *Department of Chemistry and Research Institute of Natural Sciences, Gyeongsang National University, Jinju 52828, South Korea*; orcid.org/0000-0002-4353-5131; Email: chris@gnu.ac.kr

Authors

Cheongwon Bae − *Department of Chemistry and Research Institute of Natural Sciences, Gyeongsang National University, Jinju 52828, South Korea*

Gyuyeong Jeong − *Department of Mechanical Engineering, Gyeongsang National University, Jinju 52828, South Korea*

Suhyeon Park − *Department of Chemistry and Research Institute of Natural Sciences, Gyeongsang National University, Jinju 52828, South Korea*

Yeram Kim − *Department of Chemistry and Research Institute of Natural Sciences, Gyeongsang National University, Jinju 52828, South Korea*

Mingyu Gu − *Department of Chemistry and Research Institute of Natural Sciences, Gyeongsang National University, Jinju 52828, South Korea*

Complete contact information is available at: https://pubs.acs.org/10.1021/acsomega.2c00741

https://doi.org/10.1021/acsomega.2c00741
ACS Omega 2022, 7, 17144−17150

Author Contributions

[§]C.B. and G.J. contributed equally.

Notes

The authors declare no competing financial interest.

■ ACKNOWLEDGMENTS

This work was supported by Korea Institute of Energy Technology Evaluation and Planning (Grant Number 20192050100060) from the Korea Government (MOTIE) and Basic Science Research Program (Grant Numbers 2020R1C1C1007568 and 2021R1A6A3A13044147) through the National Research Foundation of Korea funded by the Ministry of Science, ICT and Future Planning. In addition, this work was partially supported by the KBSI NFEC (Grant Number 2019R1A6C1010042) from the Ministry of Education of Korea and Nano Material Technology Development Program (Grant Number 2009-0082580).

■ REFERENCES

(1) Critoph, R. E.; Zhong, Y. Review of Trends in Solid Sorption Refrigeration and Heat Pumping Technology. *Proc. Inst. Mech. Eng., Part E* **2005**, *219*, 285−300.
(2) Klerke, A.; Christensen, C. H.; Nørskov, J. K.; Vegge, T. Ammonia for Hydrogen Storage: Challenges and Opportunities. *J. Mater. Chem.* **2008**, *18*, 2304−2310.
(3) Zhang, T. F.; Miyaoka, H.; Miyaoka, H.; Ichikawa, T.; Kojima, Y. Review on Ammonia Absorption Materials: Metal Hydrides, Halides, and Borohydrides. *ACS Appl. Energy Mater.* **2018**, *1*, 232−242.
(4) Saha, B. B.; Uddin, K.; Pal, A.; Thu, K. Emerging Sorption Pairs for Heat Pump Applications: An Overview. *JMST Adv.* **2019**, *1*, 161−180.
(5) Demirci, U. B. Ammonia Borane: An Extensively Studied, though not yet Implemented, Hydrogen Carrier. *Energies* **2020**, *13*, No. 3071.
(6) Wan, Z.; Tao, Y.; Shao, J.; Zhang, Y.; You, H. Ammonia as an Effective Hydrogen Carrier and a Clean Fuel for Solid Oxide Fuel Cells. *Energy Convers. Manage.* **2021**, *228*, No. 113729.
(7) Juangsa, F. B.; Irhamna, A. R.; Aziz, M. Production of Ammonia as Potential Hydrogen Carrier: Review on Thermochemical and Electrochemical Processes. *Int. J. Hydrogen Energy* **2021**, *46*, 14455−14477.
(8) Lan, R.; Irvine, J. T. S.; Tao, S. Ammonia and Related Chemicals as Potential Indirect Hydrogen Storage Materials. *Int. J. Hydrogen Energy* **2012**, *37*, 1482−1494.
(9) Xu, M.; Li, S.; Jin, Z.; Jiang, W.; Du, K. Experimental Investigation of the Effect of LiBr on the High-Pressure Part of a Ternary Working Fluid Ammonia Absorption Refrigeration System. *Appl. Therm. Eng.* **2021**, *186*, No. 116521.
(10) Demir, H.; Mobedi, M.; Ülkü, S. A Review on Adsorption Heat Pump: Problems and Solutions. *Renewable Sustainable Energy Rev.* **2008**, *12*, 2381−2403.
(11) Helminen, J.; Helenius, J.; Paatero, E.; Turunen, I. Adsorption Equilibria of Ammonia Gas on Inorganic and Organic Sorbents at 298.15 K. *J. Chem. Eng. Data* **2001**, *46*, 391−399.
(12) Liu, C. Y.; Aika, K.-I. Ammonia Absorption into Alkaline Earth Metal Halide Mixtures as an Ammonia Storage Material. *Ind. Eng. Chem. Res.* **2004**, *43*, 7484−7491.
(13) Askalany, A. A.; Salem, M.; Ismael, I. M.; Ali, A. H. H.; Morsy, M. G.; Saha, B. B. An Overview on Adsorption Pairs for Cooling. *Renewable Sustainable Energy Rev.* **2013**, *19*, 565−572.
(14) Jensen, P. B.; Lysgaard, S.; Quaade, U. J.; Vegge, T. Designing Mixed Metal Halide Ammines for Ammonia Storage Using Density Functional Theory and Genetic Algorithms. *Phys. Chem. Chem. Phys.* **2014**, *16*, 19732−19740.
(15) Berdiyeva, P.; Karabanova, A.; Makowska, M. G.; Johnsen, R. E.; Blanchard, D.; Hauback, B. C.; Deledda, S. In-Situ Neutron Imaging Study of NH_3 Absorption and Desorption in $SrCl_2$ within a Heat Storage Prototype Reactor. *J. Energy Storage* **2020**, *29*, No. 101388.
(16) Alothman, Z. A. A Review: Fundamental Aspects of Silicate Mesoporous Materials. *Materials* **2012**, *5*, 2874−2902.
(17) Feng, C.; E, J.; Han, W.; Deng, Y.; Zhang, B.; Zhao, X.; Han, D. Key Technology and Application Analysis of Zeolite Adsorption for Energy Storage and Heat-Mass Transfer Process: A Review. *Renewable Sustainable Energy Rev.* **2021**, *144*, No. 110954.
(18) Vikrant, K.; Kumar, V.; Kim, K.-H.; Kukkar, D. Metal−Organic Frameworks (MOFs): Potential and Challenges for Capture and Abatement of Ammonia. *J. Mater. Chem. A* **2017**, *5*, 22877−22896.
(19) Kang, D. W.; Ju, S. E.; Kim, D. W.; Kang, M.; Kim, H.; Hong, C. S. Emerging Porous Materials and Their Composites for NH_3 Gas Removal. *Adv. Sci.* **2020**, *7*, No. 2002142.
(20) Liu, Z.; An, G.; Xia, X.; Wu, S.; Li, S.; Wang, L. The Potential Use of Metal−Organic Framework/Ammonia Working Pairs in Adsorption Chillers. *J. Mater. Chem. A* **2021**, *9*, 6188−6195.
(21) Furukawa, H.; Cordova, K. E.; O'Keeffe, M.; Yaghi, O. M. The Chemistry and Applications of Metal−Organic Frameworks. *Science* **2013**, *341*, No. 1230444.
(22) Kajiwara, T.; Higuchi, M.; Watanabe, D.; Higashimura, H.; Yamada, T.; Kitagawa, H. A Systematic Study on the Stability of Porous Coordination Polymers against Ammonia. *Chem. − Eur. J.* **2014**, *20*, 15611−15617.
(23) de Lange, M. F.; Verouden, K. J. F. M.; Vlugt, T. J. H.; Gascon, J.; Kapteijn, F. Adsorption-Driven Heat Pumps: The Potential of Metal−Organic Frameworks. *Chem. Rev.* **2015**, *115*, 12205−12250.
(24) Chen, Y.; Zhang, F.; Wang, Y.; Yang, C.; Yang, J.; Li, J. Recyclable Ammonia Uptake of a MIL Series of Metal−Organic Frameworks with High Structural Stability. *Microporous Mesoporous Mater.* **2018**, *258*, 170−177.
(25) Rieth, A. J.; Dincă, M. Controlled Gas Uptake in Metal−Organic Frameworks with Record Ammonia Sorption. *J. Am. Chem. Soc.* **2018**, *140*, 3461−3466.
(26) Kim, D. W.; Kang, D. W.; Kang, M.; Lee, J. H.; Choe, J. H.; Chae, Y. S.; Choi, D. S.; Yun, H.; Hong, C. S. High Ammonia Uptake of a Metal−Organic Framework Adsorbent in a Wide Pressure Range. *Angew. Chem., Int. Ed.* **2020**, *59*, 22531−22536.
(27) Dong, X.-W.; Liu, T.; Hu, Y.-Z.; Liu, X.-Y.; Che, C.-M. Urea Postmodified in a Metal−Organic Framework as a Catalytically Active Hydrogen-Bond-Donating Heterogeneous Catalyst. *Chem. Commun.* **2013**, *49*, 7681−7683.
(28) Liu, B.; Peng, Y.; Chen, Q. Adsorption of N/S-Heteroaromatic Compounds from Fuels by Functionalized MIL-101(Cr) Metal−Organic Frameworks: The Impact of Surface Functional Groups. *Energy Fuels* **2016**, *30*, 5593−5600.
(29) Park, J. M.; Jhung, S. H. A Remarkable Adsorbent for Removal of Bisphenol S from Water: Aminated Metal−Organic Framework, MIL-101-NH_2. *Chem. Eng. J.* **2020**, *396*, No. 125224.
(30) Seredych, M.; Bandosz, T. J. Mechanism of Ammonia Retention on Graphite Oxides: Role of Surface Chemistry and Structure. *J. Phys. Chem. C* **2007**, *111*, 15596−15604.
(31) Petit, C.; Bandosz, T. J. Enhanced Adsorption of Ammonia on Metal−Organic Framework/Graphite Oxide Composites: Analysis of Surface Interactions. *Adv. Funct. Mater.* **2010**, *20*, 111−118.
(32) Zhao, Y.; Seredych, M.; Zhong, Q.; Bandosz, T. J. Superior Performance of Copper Based MOF and Aminated Graphite Oxide Composites as CO_2 Adsorbents at Room Temperature. *ACS Appl. Mater. Interfaces* **2013**, *5*, 4951−4959.
(33) Zhao, Y.; Ding, H.; Zhong, Q. Synthesis and Characterization of MOF-Aminated Graphite Oxide Composites for CO_2 Capture. *Appl. Surf. Sci.* **2013**, *284*, 138−144.
(34) Yin, Y.; Zhang, H.; Huang, P.; Xiang, C.; Zou, Y.; Xu, F.; Sun, L. Inducement of Nanoscale Cu-BTC on Nanocomposite of PPy-rGO and Its Performance in Ammonia Sensing. *Mater. Res. Bull.* **2018**, *99*, 152−160.
(35) Ghanbari, T.; Abnisa, F.; Daud, W. M. A. W. A Review on Production of Metal Organic Frameworks (MOF) for CO_2 Adsorption. *Sci. Total Environ.* **2020**, *707*, No. 135090.

https://doi.org/10.1021/acsomega.2c00741
ACS Omega 2022, 7, 17144−17150

(36) Lin, Y.; Kong, C.; Chen, L. Direct Synthesis of Amine-Functionalized MIL-101(Cr) Nanoparticles and Application for CO_2 Capture. *RSC Adv.* **2012**, *2*, 6417−6419.
(37) Jalayeri, H.; Aprea, P.; Caputo, D.; Peluso, A.; Pepe, F. Synthesis of Amino-Functionalized MIL-101(Cr) MOF for Hexavalent Chromium Adsorption from Aqueous Solutions. *Environ. Nanotechnol. Monit. Manage.* **2020**, *14*, No. 100300.
(38) Cullity, B. D.; Stock, S. R. *Elements of X-ray Diffraction*, Prentice-Hall, 2001; pp 96−102.
(39) Petit, C.; Bandosz, T. J. MOF-Graphite Oxide Composites: Combining the Uniqueness of Graphene Layers and Metal−Organic Frameworks. *Adv. Mater.* **2009**, *21*, 4753−4757.
(40) Zhou, X.; Huang, W.; Shi, J.; Zhao, Z.; Xia, Q.; Li, Y.; Wang, H.; Li, Z. A Novel MOF/Graphene Oxide Composite GrO@MIL-101 with High Adsorption Capacity for Acetone. *J. Mater. Chem. A* **2014**, *2*, 4722−4730.
(41) Zhou, F.; Zhou, J.; Gao, X.; Kong, C.; Chen, L. Facile Synthesis of MOFs with Uncoordinated Carboxyl Groups for Selective CO_2 Capture via Postsynthetic Covalent Modification. *RSC Adv.* **2017**, *7*, 3713−3719.
(42) Hasan, Z.; Tong, M.; Jung, B. K.; Ahmed, I.; Zhong, C.; Jhung, S. H. Adsorption of Pyridine over Amino-Functionalized Metal−Organic Frameworks: Attraction via Hydrogen Bonding versus Base-Base Repulsion. *J. Phys. Chem. C* **2014**, *118*, 21049−21056.
(43) Chandra, V.; Kim, K. S. Highly Selective Adsorption of Hg^{2+} by a Polypyrrole-Reduced Graphene Oxide Composite. *Chem. Commun.* **2011**, *47*, 3942−3944.
(44) Wang, J.-W.; Qiao, L.-Z.; Nie, H.-D.; Huang, H.-H.; Li, Y.; Yao, S.; Liu, M.; Zhang, Z.-M.; Kang, Z.-H.; Lu, T.-B. Facile Electron Delivery from Graphene Template to Ultrathin Metal−Organic Layers for Boosting CO_2 Photoreduction. *Nat. Commun.* **2021**, *12*, No. 813.
(45) Brown, S. D. M.; Jorio, A.; Dresselhaus, M. S.; Dresselhaus, G. Observations of the D-Band Feature in the Raman Spectra of Carbon Nanotubes. *Phys. Rev. B* **2001**, *64*, No. 073403.
(46) Kudin, K. N.; Ozbas, B.; Schniepp, H. C.; Prud'homme, R. K.; Aksay, I. A.; Car, R. Raman Spectra of Graphite Oxide and Functionalized Graphene Sheets. *Nano Lett.* **2008**, *8*, 36−41.
(47) Li, X.; Pi, Y.; Xia, Q.; Li, Z.; Xiao, J. TiO_2 Encapsulated in Salicylaldehyde-NH_2-MIL-101(Cr) for Enhanced Visible Light-Driven Photodegradation of MB. *Appl. Catal., B* **2016**, *191*, 192−201.
(48) Wu, H.; Wang, Z.-M.; Kumagai, A.; Endo, T. Amphiphilic Cellulose Nanofiber-Interwoven Graphene Aerogel Monolith for Dyes and Silicon Oil Removal. *Compos. Sci. Technol.* **2019**, *171*, 190−198.
(49) Thomson, W. 4. On the Equilibrium of Vapour at a Curved Surface of Liquid. *Proc. R. Soc.* **1872**, *7*, 63−68.
(50) Fisher, L. R.; Gamble, R. A.; Middlehurst, J. The Kelvin Equation and the Capillary Condensation of Water. *Nature* **1981**, *290*, 575−576.
(51) Kruk, M.; Jaroniec, M.; Sayari, A. Application of Large Pore MCM-41 Molecular Sieves to Improve Pore Size Analysis Using Nitrogen Adsorption Measurements. *Langmuir* **1997**, *13*, 6267−6273.

https://doi.org/10.1021/acsomega.2c00741
ACS Omega 2022, 7, 17144−17150